January 2010

A multirate field construction technique for efficient modeling of the fields and forces within inverter-fed induction machines

Wu Dezheng

S. D. Pekarek

Dezheng, Wu and Pekarek, S. D., "A multirate field construction technique for efficient modeling of the fields and forces within inverter-fed induction machines" (2010). *Department of Electrical and Computer Engineering Faculty Publications.* Paper 50.
http://dx.doi.org/http://dx.doi.org/10.1109/TEC.2009.2032606

A Multirate Field Construction Technique for Efficient Modeling of the Fields and Forces Within Inverter-Fed Induction Machines

Dezheng Wu and Steven D. Pekarek, *Member, IEEE*

***Abstract*—In recent research, a field construction technique (FCT) was derived to enable more efficient evaluation of the magnetic fields and forces within induction machines. Using the FCT, the results of two finite-element (FE) solutions are used to establish basis functions for the flux densities in the airgap of the machine. The basis functions are then used to predict the magnetic fields and forces under arbitrary stator excitation. In this paper, a multirate FCT (MRFCT) is proposed to enable efficient FCT modeling of machines that are connected to power electronic converters. Within the MRFCT, the low- and high-frequency components of the stator current are partitioned. The partitioned currents are then used to calculate the flux density and forces at time steps commensurate with the respective low- and high-frequency dynamics. It is shown that applying the MRFCT, the forces and fields of a machine connected to a power electronic circuit can be obtained at a small fraction of the time required for a coupled FE/circuit model.**

***Index Terms*—Electromagnetic fields and forces, field construction, finite element methods, induction machines, induction motor drives.**

I. Introduction

NUMEROUS researchers have explored the use of finite-element-based techniques to model induction machines [1]–[11]. With advances in drive systems, there has been a focus on developing methods to couple finite-element analysis (FEA) models with external circuits to simulate overall drive system behavior. For the induction machine, coupling circuit/FEA has been considered in [1]–[6]. A more general view of machine/circuit coupling has been documented in [12]–[18].

In broad terms, the methods of coupling FEA models with external circuits can be classified into indirect (weak) coupling methods (ICM) and direct (strong) coupling methods (DCM). Within the ICM [1]–[4], FEA is used to calculate lumped circuit parameter values for the machine. The parameter values are then provided to a circuit simulator to establish the circuit response. The circuit response is used to obtain the current, which is the input to the FEA model. In effect, indirect methods solve the coupled field/circuit model by separating the field and circuit equations.

Manuscript received December 15, 2009; revised May 4, 2009. First published December 8, 2009; current version published February 17, 2010. This work was supported by the Electric Ship Research and Development Consortium (ESRDC) under Contract N00014-02-1-0623 with the Office of Naval Research. Paper no. TEC-00496-2008.

D. Wu is with the ABB US Corporate Research Center, Raleigh, NC 27606-5202 USA.

S. D. Pekarek is with Purdue University, West Lafayette, IN 47907 USA.

Color versions of one or more of the figures in this paper are available online at http://ieeexplore.ieee.org.

Digital Object Identifier 10.1109/TEC.2009.2032606

In the DCMs applied to induction machines [5], [6], the dynamics of the circuit and FEA are considered simultaneously. One approach to DCM is to form a full system of equations for the machine/circuit by augmenting the circuit's mesh or nodal equations to the field equations of the FEA [5], [6]. In such an approach, the currents and magnetic vector potentials are both treated as unknowns and solved simultaneously. In an alternative approach that has been applied to switched reluctance machines, the winding voltage equations are expressed in state model form with the winding flux linkages as state variables [12], [13]. The flux linkages calculated from the solution of the circuit equation are provided to the FEA model to solve the so-called inverse problem (finding stator current from stator flux linkage). The winding currents are then used to update the state model.

Despite the considerable effort that has been spent on developing FEA/circuit models, a shortcoming remains that the coupled models require significant computational resources, particularly for machines in which time-varying FEA is utilized. A so-called field construction technique (FCT) was introduced in [19] to reduce the computational burden of field-based analysis of induction machinery. In the FCT approach, two FEA evaluations are used to determine the normal and tangential components of the flux density in the airgap under single-winding excitation and zero rotor speed. The FEA results are then used to establish basis functions of the airgap flux density. Using the basis functions, fields and forces acting inside the machine are predicted under arbitrary stator excitation and rotor speed [19]. In [20] and [21], the current-input-based FCT was extended to enable stator voltage as the model input. Therein, so-called flux linkage basis functions are introduced to predict the stator flux linkages under arbitrary voltage excitation. Stator currents are treated as state variables that are calculated by integrating stator voltage equations.

The FCTs focused on the modeling of the machine dynamics in [19]–[21]. In this paper, a focus is placed on the coupled modeling of machine/inverter systems. To efficiently model machine/inverter performance, a multirate FCT (MRFCT) is developed. Within the MRFCT, stator currents are partitioned into low- and high-frequency components. Separate field constructions (low frequency and high frequency) are performed using the partitioned current components, respectively. The field outputs are then added together to obtain the overall fields and forces acting within the machine.

The electrical inputs to the MRFCT model are the stator winding voltages applied to the machine which is the same input used for some of the direct FEA solvers and also lumped-parameter

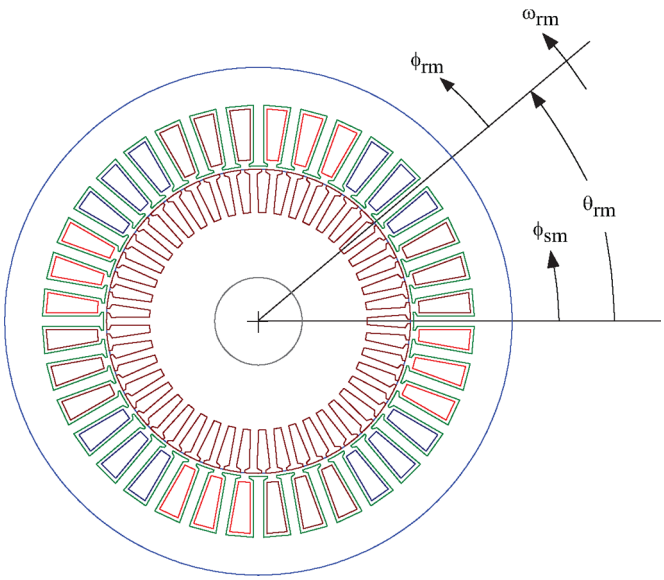

Fig. 1. Cross-sectional view of the induction machine.

models. Since the stator voltage is an input, coupling of the MRFCT model with an inverter is relatively straightforward using techniques that are described in [22]. In addition, although three FEA evaluations are required to establish basis functions used in the MRFCT, the FEA evaluations are straightforward and are performed at an arbitrary fixed rotor position using a single stator current as an input. Finally, the MRFCT is shown to yield a tremendous reduction in computational effort compared to an FEA model coupled with an inverter. For the studies shown herein, the dynamics of a 3-phase machine coupled to a sine-triangle-based inverter solved at a rate of 2400 times slower than real time using MRFCT on a desktop PC. In contrast, a corresponding commercial 2-D FEA solved at a rate of 745,200 times slower than real time. Despite the significant reduction in computational effort, the stator currents and torque obtained by MRFCT are nearly identical to that obtained from the FEA (in both the time and frequency domains).

II. Machine Description, Force Calculation, and Assumptions

The cross-sectional view of the induction machine studied in this paper is shown in Fig. 1. It is a 3-phase, 60-Hz, 4-pole, 5-hp squirrel-cage induction machine that contains 36 stator slots, 45 rotor slots, and 22 conductors per stator slot. The stator windings are wound at a full pitch. Geometry and material properties of the machine are described in Appendix A.

In Fig. 1, the angles ϕ_{sm} and ϕ_{rm} are used to denote the angular position along the stator circumference and rotor circumference, respectively. Angle θ_{rm} is the mechanical rotor position. The mechanical angular velocity of the rotor is ω_{rm}. Based upon the definitions, the relationship

$$\phi_{sm} = \phi_{rm} + \theta_{rm} \tag{1}$$

is obtained.

The Maxwell stress tensor (MST) method is used to calculate forces inside the machine, where the tangential and normal force densities in airgap are expressed as [23]

$$f_t = \frac{B_n B_t}{\mu_0} \tag{2}$$

$$f_n = \frac{\left(B_n^2 - B_t^2\right)}{2\mu_0} \tag{3}$$

where B_n and B_t are normal and tangential components of the flux density, respectively, and μ_0 is the permeability of air. Thus, the electromagnetic torque is obtained by integrating tangential force density along the contour in the airgap, i.e.

$$T_{\rm e} = \frac{R^2\, l}{\mu_0} \int_0^{2\pi} B_n B_t d\phi_{sm} \tag{4}$$

where l is the effective stack length and R is the radius of the integration contour. The circular integration contour is established in the middle of the airgap to minimize numerical error [24].

The following assumptions have been made for the analysis in this paper.

1) The machine is assumed to operate in the linear magnetic range. In addition, hysteresis and eddy currents in the stator and rotor iron are neglected.
2) The stator teeth and rotor teeth are assumed to be rigid, i.e., no deformation due to radial and tangential force occurs in these parts.
3) The flux density in the axial direction is zero, and therefore, end effects are neglected.

III. Field Construction Technique

The FCT for induction machines in which stator voltage is the input is briefly reviewed in this section. Detailed derivation and explanation are presented in [19]–[21]. The FCT is established based upon the assumption that the machine is operated in the linear magnetic region, which is consistent with the assumption used in many models. Since the machine is assumed to operate in the linear magnetic range, the flux density at any point in the machine can be expressed as the sum of the flux density due to the stator current and the flux density due to the rotor current, respectively. In other words, superposition is applied to calculate flux density. In FCT, the normal and tangential components of the flux density are expressed in terms of stator and rotor quantities, i.e.

$$B_n(\phi_{sm}) = B_{ns}(\phi_{sm}) + B_{nr}(\phi_{sm}, \theta_{rm}) \tag{5}$$

$$B_t(\phi_{sm}) = B_{ts}(\phi_{sm}) + B_{tr}(\phi_{sm}, \theta_{rm}) \tag{6}$$

where B_{ns} and B_{ts} are normal and tangential components of the flux density directly generated by stator current and B_{nr} and B_{tr} are normal and tangential components of the flux density generated by rotor currents.

Stator and rotor basis functions are used to determine flux densities within the FCT model. The stator basis functions are characterized using a static FEA solution under the excitation $i_{as} = 1$ A, $i_{bs} = i_{cs} = 0$. The normal and tangential components of the flux density in the airgap are obtained and defined as stator basis functions ($k_{ns}(\phi_{sm})$ and $k_{ts}(\phi_{sm})$). The basis function $k_{ns}(\phi_{sm})$ is for the normal component and $k_{ts}(\phi_{sm})$

is for the tangential component. In the computer program, the integration contour is discretized into p equally distributed points. Hence, the stator basis functions are expressed as two p-by-1 vectors. The flux density directly generated by stator current is obtained by

$$B_{xs}\left(\phi_{sm}\right) = i_{as}k_{xs}\left(\phi_{sm}\right) + i_{bs}k_{xs}\left(\phi_{sm} - \frac{2}{P}\frac{2\pi}{3}\right) + i_{cs}k_{xs}\left(\phi_{sm} - \frac{2}{P}\frac{4\pi}{3}\right) \tag{7}$$

where x may be n or t, and P is the number of poles.

Rotor basis functions ($k_{nr}(\phi_{rm}, t)$ and $k_{tr}(\phi_{rm}), t)$) are characterized using a transient FEA solution with rotor position fixed. A discrete impulse is used as the phase-a current input to the FEA model. The impulse input signal has a value of I_0 at $t = 0$, and 0 elsewhere, i.e.

$$i_{as}(t) = \begin{cases} I_0, & t = 0 \\ 0, & t \neq 0. \end{cases} \tag{8}$$

The characterization of the rotor basis functions requires the FEA model to run over a period of time in order to capture sufficient data for subsequent studies. During the calculation time, all the normal and tangential components of the airgap flux density at $t \geq 0$ are recorded as $B_{nid}(t)$ and $B_{tid}(t)$. Since the rotor basis functions are the desired knowledge, the flux densities contributed by the stator current ($i_{as}k_{ns}$ and $i_{as}k_{ts}$) are subtracted. Specifically, using the previously established stator basis functions, the normal and tangential components of the flux density generated by rotor current, B_{nr} and B_{tr}, are represented by

$$B_{nr} = B_{nid} - i_{as}k_{ns} \tag{9}$$

$$B_{tr} = B_{tid} - i_{as}k_{ts} \tag{10}$$

where B_{nr} and B_{tr} are then divided by I_0 to obtain the unit rotor impulse responses k_{nr} and k_{tr}

$$k_{nr} = \frac{B_{nr}}{I_0} \tag{11}$$

$$k_{tr} = \frac{B_{tr}}{I_0}. \tag{12}$$

The unit impulse responses are then defined as the rotor basis functions. Since rotor basis functions are expressed as unit impulse responses, discrete-time convolution [25] is used to obtain B_{nr} and B_{tr} under arbitrary excitations, i.e.

$$B_{x\mathrm{r}}\left(\phi_{rm}, t\right) = i_{as}(t) * k_{x\mathrm{r}}\left(\phi_{rm}, t\right) + i_{bs}(t) * k_{x\mathrm{r}}\left(\phi_{rm} - \frac{2}{P}\frac{2\pi}{3}, t\right) + i_{cs}(t) * k_{x\mathrm{r}}\left(\phi_{rm} - \frac{2}{P}\frac{4\pi}{3}, t\right) \tag{13}$$

where $*$ denotes convolution. A description of discrete-time convolution is briefly reviewed in Appendix B. In the computer program, the convolution in (13) is evaluated in the discrete-time form, and the overall flux density in terms of the stator coordinate is expressed as

$$\begin{aligned} B_x\left(\phi_{sm}, t_k\right) &= i_{as}\left(t_k\right)k_{xs}\left(\phi_{sm}\right) \\ &\quad + i_{bs}\left(t_k\right)k_{xs}\left(\phi_{sm} - \frac{2}{P}\frac{2\pi}{3}\right) \\ &\quad + i_{cs}\left(t_k\right)k_{xs}\left(\phi_{sm} - \frac{2}{P}\frac{4\pi}{3}\right) \\ &\quad + \sum_{u=1}^{k} i_{as}\left(t_u\right)k_{x\mathrm{r}}\left(\phi_{sm} - \Delta\theta_{rm}, \Delta t\right) \\ &\quad + \sum_{u=1}^{k} i_{bs}\left(t_u\right)k_{x\mathrm{r}}\left(\phi_{sm} - \Delta\theta_{rm} - \frac{2}{P}\frac{2\pi}{3}, \Delta t\right) \\ &\quad + \sum_{u=1}^{k} i_{cs}\left(t_u\right)k_{x\mathrm{r}}\left(\phi_{sm} - \Delta\theta_{rm} - \frac{2}{P}\frac{4\pi}{3}, \Delta t\right) \end{aligned} \tag{14}$$

where $\Delta\theta_{rm} = \theta_{rm}(t_k) - \theta_{rm}(t_u)$ and $\Delta t = t_k - t_u$. As an example to illustrate how this is performed, it is convenient to assume that stator current $i_{as} = 10\cos(377t)$, $i_{bs} = 0$, $i_{cs} = 0$, and the rotor speed $\omega_{rm} = 17.45$ rad/s $= 1000°$/s. The step size is 0.001 s, which means the rotor angle ω_{rm} has an incremental of 1°/step. Here, B_n at $\phi_{sm} = 60°$, and time t_k can be calculated using (14) as

$$\begin{aligned} B_n\left(60°, t_k\right) &= k_{ns}(60°)i_{as}(t_k) + k_{nr}(60°, 0\,\mathrm{s})i_{as}(t_k) \\ &\quad + k_{nr}(59°, 0.001\,\mathrm{s})i_{as}(t_k - 0.001\,\mathrm{s}) \\ &\quad + k_{nr}(58°, 0.002\,\mathrm{s})i_{as}(t_k - 0.002\,\mathrm{s}) + \cdots \end{aligned} \tag{15}$$

The second term on the right side in (15) is the rotor flux density due to $i_{as}(t_k)$, and the third term is due to the input at the previous step $i_{as}(t_k - 0.001$ s).

In (14), stator currents are the input to calculate magnetic flux density, which is then used in (4) to calculate torque. To incorporate the stator windings, and thus, external circuits, the voltage equations for the stator windings are expressed in the arbitrary reference frame [22]

$$\mathbf{v}_{qd0s} = r_s\mathbf{i}_{qd0s} + \boldsymbol{\omega}\boldsymbol{\lambda}_{qd0s} + \frac{d\boldsymbol{\lambda}_{qd0s}}{dt} \tag{16}$$

where r_s is the stator resistance and

$$\mathbf{f}_{qd0s} = \begin{bmatrix} f_{qs} & f_{ds} & f_{0s} \end{bmatrix}^T \tag{17}$$

where f can be v, i, or λ. In (16),

$$\boldsymbol{\omega} = \begin{bmatrix} 0 & \omega & 0 \\ -\omega & 0 & 0 \\ 0 & 0 & 0 \end{bmatrix} \tag{18}$$

where ω is the angular speed of the arbitrary reference frame. To solve (16), the relationship between stator current and flux linkage is required. To obtain this relation, the stator flux linkage

equations are expressed in the form

$$\lambda_{qs} = L_{ss} i_{qs} + \lambda_{qs,\mathrm{r}} \tag{19}$$

$$\lambda_{ds} = L_{ss} i_{ds} + \lambda_{ds,\mathrm{r}} \tag{20}$$

$$\lambda_{0s} = L_{ls} i_{0s} \tag{21}$$

where $L_{ss} = L_{ls} + L_M$, L_{ls} is the stator leakage inductance, and L_M is the magnetizing inductance. In (19)–(21), the first terms on the right side of the equations are due to stator current, and the second terms ($\lambda_{qs,r}$ and $\lambda_{ds,r}$) represent the portion of the stator flux linkage that is due to the rotor current. The FEA solutions used to obtain the stator and rotor flux density basis functions are also used to obtain the parameters in (19)–(21). Specifically,

$$L_{ss} = \lambda_{as,ST} - \lambda_{bs,ST} \tag{22}$$

$$L_{\mathrm{ls}} = \lambda_{as,ST} + 2\lambda_{bs,ST} \tag{23}$$

where $\lambda_{as,ST}$ and $\lambda_{bs,ST}$ are the flux linkages of the phase-a and -b windings in the static FEA solution used to obtain the stator basis functions.

To characterize the flux linkage basis function that is used to calculate $\lambda_{qs,r}$ and $\lambda_{ds,r}$, one uses the same transient FEA solution used to obtain (11) and (12). In the transient FEA program, the rotor is stationary, $i_{bs} = i_{cs} = 0$, and i_{as} is the discrete-time impulse signal described in (8). The stator flux linkage results obtained from the transient solution are represented as $\lambda_{as}(t)$, $\lambda_{bs}(t)$, and $\lambda_{cs}(t)$, respectively. Due to symmetry, $\lambda_{bs}(t) = \lambda_{cs}(t)$.

Using a stationary reference frame for basis function characterization, the *qs*-axis flux linkage and current are expressed as

$$\lambda^s_{qs} = \frac{(2\lambda_{as} - \lambda_{bs} - \lambda_{cs})}{3} \tag{24}$$

$$i^s_{qs} = \frac{2i_{as}}{3} \tag{25}$$

where the superscript s indicates that the variables are in the stationary reference frame. It is noted that since i_{as} is an impulse, i^s_{qs} is also an impulse signal with the impulse amplitude $2I_0/3$.

Since the flux linkage components due to rotor current are of interest, the component due to stator current is subtracted. The result is then divided by the amplitude of the impulse ($2I_0/3$) to obtain the flux linkage basis function

$$k_\lambda(t) = \frac{\lambda^s_{qs}(t) - L_{ss} i^s_{qs}(t)}{2I_0/3}. \tag{26}$$

Using the flux linkage basis function, one may express $\lambda_{qs,r}$ and $\lambda_{ds,r}$ in the stationary reference frame as

$$\begin{bmatrix} \lambda^s_{qs,\mathrm{r}} \\ \lambda^s_{ds,\mathrm{r}} \end{bmatrix} = k_\lambda * \begin{bmatrix} i^s_{qs} \\ i^s_{ds} \end{bmatrix}. \tag{27}$$

Numerically, (27) is evaluated using

$$\begin{bmatrix} \lambda^s_{qs,\mathrm{r}}(t_k) \\ \lambda^s_{ds,\mathrm{r}}(t_k) \end{bmatrix} = \sum_{u=1}^{k} k_\lambda(t_k - t_u) \begin{bmatrix} i^s_{qs}(t_u) \\ i^s_{qs}(t_u) \end{bmatrix}. \tag{28}$$

Applying a reference frame transformation to (28) to express the rotor components of the stator flux linkage in the arbitrary reference frame and substituting into (19)–(21), the stator flux linkages are expressed using

$$\begin{bmatrix} \lambda_{qs}(t_k) \\ \lambda_{ds}(t_k) \end{bmatrix} = L_{ss} \begin{bmatrix} i_{qs}(t_k) \\ i_{ds}(t_k) \end{bmatrix} + \sum_{u=1}^{k} \mathbf{K}(t_k,\, t_u)\, k_\lambda(t_k - t_u) \begin{bmatrix} i_{qs}(t_u) \\ i_{ds}(t_u) \end{bmatrix} \tag{29}$$

where

$$\mathbf{K}(t_k,\, t_u) = \begin{bmatrix} \cos\left(\Delta\theta - \frac{P}{2}\Delta\theta_{rm}\right) & -\sin\left(\Delta\theta - \frac{P}{2}\Delta\theta_{rm}\right) \\ \sin\left(\Delta\theta - \frac{P}{2}\Delta\theta_{rm}\right) & \cos\left(\Delta\theta - \frac{P}{2}\Delta\theta_{rm}\right) \end{bmatrix} \tag{30}$$

$$\Delta\theta = \theta\,(t_k) - \theta\,(t_u) \tag{31}$$

and angle θ is the position of the reference frame. The matrix $\boldsymbol{K}(t_k, t_u)$ represents the variable transformation between reference frames [22].

To implement the voltage-based FC model, one of a number of integration algorithms can be applied. As an example, the backward-Euler method is used to solve (16) numerically. If one selects the stationary reference frame to implement the model, and uses the relationship between stator current and stator flux linkage of (29), the update formula for stator current can be expressed as [20], [21]

$$\begin{bmatrix} i^s_{qs}(t_{k+1}) \\ i^s_{ds}(t_{k+1}) \end{bmatrix} = \frac{1}{L}\left(L_{ss} \begin{bmatrix} i^s_{qs}\,(t_k) \\ i^s_{ds}\,(t_k) \end{bmatrix} + \sum_{u=1}^{k} \mathbf{A} \begin{bmatrix} i^s_{qs}(t_u) \\ i^s_{ds}(t_u) \end{bmatrix} + h \begin{bmatrix} v^s_{qs}(t_{k+1}) \\ v^s_{ds}(t_{k+1}) \end{bmatrix} \right) \tag{32}$$

where $L = L_{ss} + k_\lambda(0) + hr_s$, h being the step size, and

$$\mathbf{A} = \left[k_\lambda(t_k - t_u)\mathbf{K}(t_k, t_u) - k_\lambda(t_{k+1} - t_u)\mathbf{K}(t_{k+1}, t_u)\right]. \tag{33}$$

Effectively, in (32), the stator current is the state variable, and is calculated according to the voltage, rotor speed, and flux linkage values in the previous step. The i_{0s} is calculated using

$$i_{0s}(t_{k+1}) = \frac{L_{ss} i_{0s}(t_k) + h \times v_{0s}(t_{k+1})}{L_{ss} + h \times r_s}. \tag{34}$$

The stator currents are then transformed to *abc* variables, which are used to evaluate the flux density in the airgap. The overall field construction process with stator voltage as an input is illustrated in Fig. 2.

IV. Multirate FCT

Equations (14) and (32)–(34) represent the voltage-input-based FCT. Using voltage as an input, the FCT-based model can be coupled directly to inverter models that are voltage-output, current-input based. For example, given the connection shown in Fig. 3, (neglecting the voltage drop across switches or diodes for purpose of explanation), the stator voltages of the induction

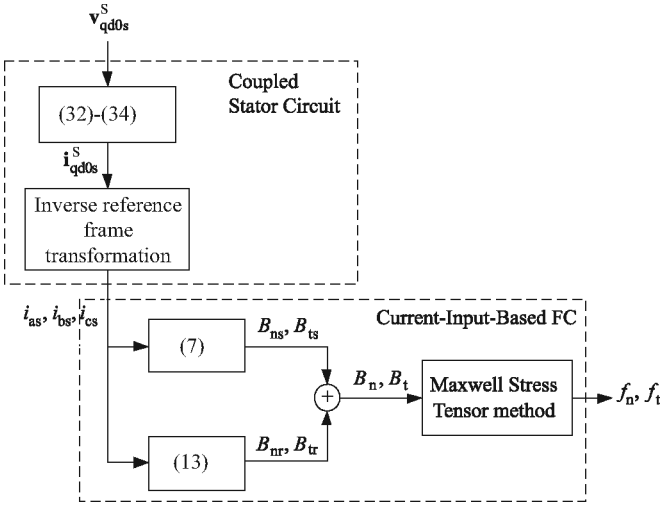

Fig. 2. Overall field construction process using stator voltage as input.

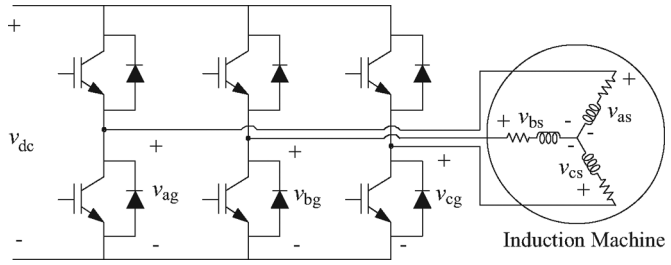

Fig. 3. Induction machine fed by an inverter.

machine can be expressed in terms of lower switch voltages as [22]

$$v_{as} = \frac{2}{3}v_{ag} - \frac{1}{3}v_{bg} - \frac{1}{3}v_{cg} \tag{35}$$

$$v_{bs} = \frac{2}{3}v_{bg} - \frac{1}{3}v_{ag} - \frac{1}{3}v_{cg} \tag{36}$$

$$v_{cs} = \frac{2}{3}v_{cg} - \frac{1}{3}v_{ag} - \frac{1}{3}v_{bg} \tag{37}$$

where the lower switch voltages of each phase leg are determined by the control applied to the inverter. For example, in the case of a sine–triangle switching strategy, the terminal voltages of the induction machine are

$$v_{xg} = \begin{cases} v_{dc}, & \text{if } d_x \geq v_{\text{tri}} \\ 0, & \text{if } d_x < v_{\text{tri}} \end{cases} \tag{38}$$

where v_{xg} is the lower switch phase-leg voltage (x may be a, b, or c) and v_{tri} is the voltage of the triangle wave. The triangle wave varies between -1 and 1 with a frequency much higher than the duty cycles.

To model the machine/inverter performance, the stator voltages are obtained analytically using (35)–(37), and are transformed to the stationery reference frame. The result ($\mathbf{v}^{s}_{qd0s}$) is then applied in (32)–(34) to calculate the stator current, which is then used in the next step to calculate the airgap flux densities and forces within the machine using (14) and (4).

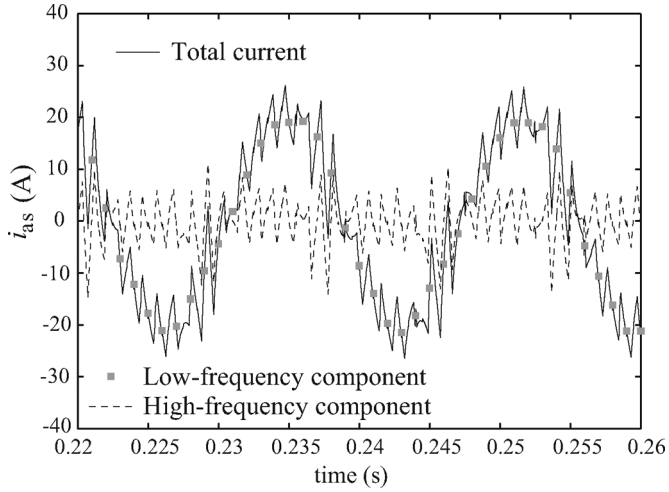

Fig. 4. Phase-a stator current.

For switched systems, direct application of an FCT itself can be computationally intense. The computational burden of FCT is dominated by the discrete-time convolution evaluations in the flux density calculations of (14). Viewing the summations in (14), one can assess that to compute the flux densities at p points around the contour in the airgap using a discrete-time impulse response with N samples requires $O(pN^2)$ operations.

A problem in inverter/machine application is that in order to create a model that can compute the slow-varying response, the discrete-time convolution must be taken over a relatively long period of time. In order to create a model that accurately captures the fast-varying response due to switching, the impulse response must be established at a sufficiently high sampling rate. Thus, to model both fast- and slow dynamics, one needs to perform convolution using a high sampling rate over long periods of time. As an example, if the dynamics of the machine are desired over a 1 s time interval, and one uses a 10 μs step size to capture the dynamic behavior at $p = 1000$ points in the airgap, the number of operations is $O(10^{13})$.

To reduce computational effort, it is convenient to consider the behavioral aspects of the system. Fast dynamics are short-lived and so there is no need to consider their impact over long intervals of time. Thus, the convolution can be truncated when considering the fast dynamics. In contrast, the slow dynamics do not change over small intervals of time. Therefore, one can reduce the sampling rate when modeling the slow dynamics of the system.

Based upon these considerations, an MRFCT is proposed to partition the field construction into a slow subsystem and a fast subsystem. To do so, the flux density components are first expressed as

$$B_n = B_{n,\text{lf}} + B_{n,\text{hf}} \tag{39}$$

$$B_t = B_{t,\text{lf}} + B_{t,\text{hf}} \tag{40}$$

where $B_{n,\text{lf}}$, $B_{t,\text{lf}}$ are the field construction results of the slow subsystem, and $B_{n,\text{hf}}$, $B_{t,\text{hf}}$ that of the fast subsystem. The flux densities in (39) and (40) are established using the same calculations outlined in (14) and Fig. 2. However, $B_{n,\text{lf}}$, $B_{t,\text{lf}}$ are

calculated using a step size commensurate with low-frequency dynamics, while $B_{n,\mathrm{hf}}$, $B_{t,\mathrm{hf}}$ are calculated using a time step that is sufficient to obtain high-frequency (switching-induced) dynamics. To accomplish this partitioning, the stator current is first decomposed into the low-frequency and the high-frequency components, respectively. In order to aid in explanation, an example current i_{as} is shown in Fig. 4.

The stator current shown in Fig. 4 contains a low-frequency component around 60 Hz and a high-frequency component around 1 kHz, which is due to switching. In order to obtain the low-frequency component, i_{as} is sampled with a time step of h_{slow} and the result is shown as square marks in Fig. 4. The high-frequency component is then obtained by

$$i_{as,\mathrm{hf}} = i_{as} - i'_{as,\mathrm{lf}} \tag{41}$$

where $i'_{as,\mathrm{lf}}$ is the linear spline interpolation result of $i_{as,\mathrm{lf}}$. The high-frequency component of the phase-a stator current is shown in Fig. 4. The stator current components of phase-b ($i_{bs,\mathrm{lf}}$, $i_{bs,\mathrm{hf}}$) and -c ($i_{cs,\mathrm{lf}}$, $i_{cs,\mathrm{hf}}$) are partitioned using the same method.

With the stator currents partitioned, the slow subsystem is evaluated using (14) with $i_{as,\mathrm{lf}}$, $i_{bs,\mathrm{lf}}$, and $i_{cs,\mathrm{lf}}$ as the input. The outputs are $B_{n,\mathrm{lf}}$ and $B_{\mathrm{t,lf}}$. The step size of the slow system convolution is h_{slow} (sampling rate of 1/ h_s).

To calculate the high-frequency response, $B_{n,\mathrm{hf}}$ and $B_{t,\mathrm{hf}}$ are obtained with $i_{as,\mathrm{hf}}$, $i_{bs,\mathrm{hf}}$, and $i_{cs,\mathrm{hf}}$ as the input. The step size of the fast system convolution is h_{fast} (sampling rate of 1/h_f). In evaluating (14) for the high-frequency response, the consideration that the fast dynamics are short-lived is applied and the convolution is truncated. Specifically, within the discrete-time convolution, only the last N_f samples of the $i_{as,\mathrm{hf}}$, $i_{bs,\mathrm{hf}}$, and $i_{cs,\mathrm{hf}}$ are included, i.e.

$$\begin{aligned}
&B_{x,\mathrm{hf}}\left(\phi_{sm}, t_k\right) \\
&= i_{as,\mathrm{hf}}\left(t_k\right) k_{xs}\left(\phi_{sm}\right) + i_{bs,\mathrm{hf}}\left(t_k\right) k_{xs}\left(\phi_{sm} - \frac{2}{P}\frac{2\pi}{3}\right) \\
&\quad + i_{cs,\mathrm{hf}}\left(t_k\right) k_{xs}\left(\phi_{sm} - \frac{2}{P}\frac{4\pi}{3}\right) \\
&\quad + \sum_{u=j}^{k} i_{as,\mathrm{hf}}\left(t_u\right) k_{xr}\left(\phi_{sm} - \Delta\theta_{\mathrm{rm}},\, \Delta t\right) \\
&\quad + \sum_{u=j}^{k} i_{bs,\mathrm{hf}}\left(t_u\right) k_{xr}\left(\phi_{sm} - \Delta\theta_{rm} - \frac{2}{P}\frac{2\pi}{3},\, \Delta t\right) \\
&\quad + \sum_{u=j}^{k} i_{cs,\mathrm{hf}}\left(t_u\right) k_{xr}\left(\phi_{sm} - \Delta\theta_{\mathrm{rm}} - \frac{2}{P}\frac{4\pi}{3},\, \Delta t\right)
\end{aligned} \tag{42}$$

where $j = k - N_f + 1$. For example, setting $N_f + 100$ means only the latest 100 steps of $i_{as,\mathrm{hf}}$, $i_{bs,\mathrm{hf}}$, and $i_{cs,\mathrm{hf}}$ are considered in the fast subsystem. The influence of $i_{as,\mathrm{hf}}$, $i_{bs,\mathrm{hf}}$, and $i_{cs,\mathrm{hf}}$ before step j is neglected since their impact has decayed to negligible values. Selecting N_f is an engineering decision that must be made by the system analyst, much like selecting the time step of a numerical integration algorithm. In the example systems that we have considered, it has been found that setting N_f to capture a single cycle of the high-frequency switching period yields reasonable accuracy.

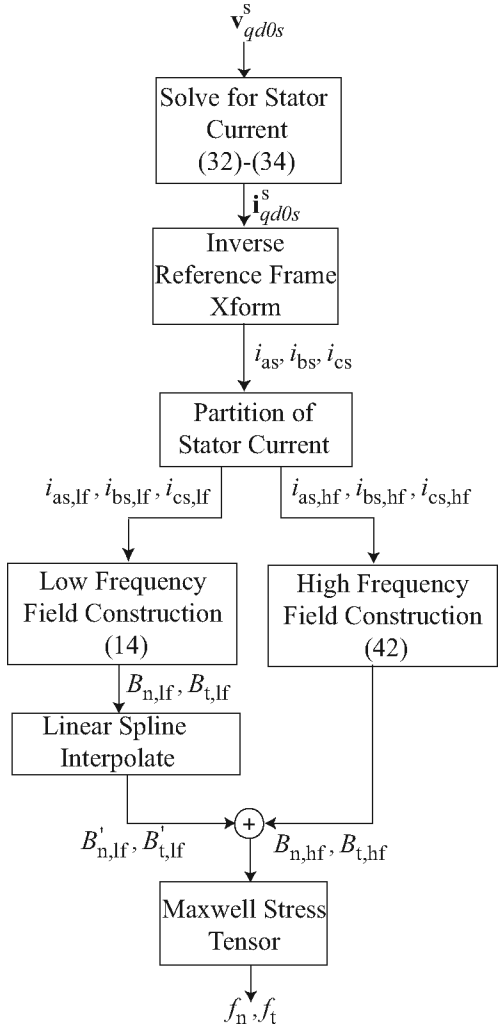

Fig. 5. Block diagram of the MRFCT.

It is noted that within (42), a set of rotor basis functions with step size h_{fast} is used to calculate $B_{n,\mathrm{hf}}$ and $B_{t,\mathrm{hf}}$. To obtain the rotor basis functions used in the fast subsystem calculations, a third FEA evaluation is required as part of the initial basis function characterization. The procedure is the same transient FEA as that described in Section III, except that a time step h_{fast} is used in the transient FEA model and only N_f samples are collected.

Within the MRFCT, total flux density components are obtained by summing the field construction results of low-frequency part and high-frequency part as in (39) and (40). A block diagram of MRFCT is illustrated in Fig. 5.

V. Results

To demonstrate the proposed MRFCT, the simulation of the induction machine fed by a three-phase inverter shown in Fig. 3 is given. A sine–triangle pulse width modulation (PWM)

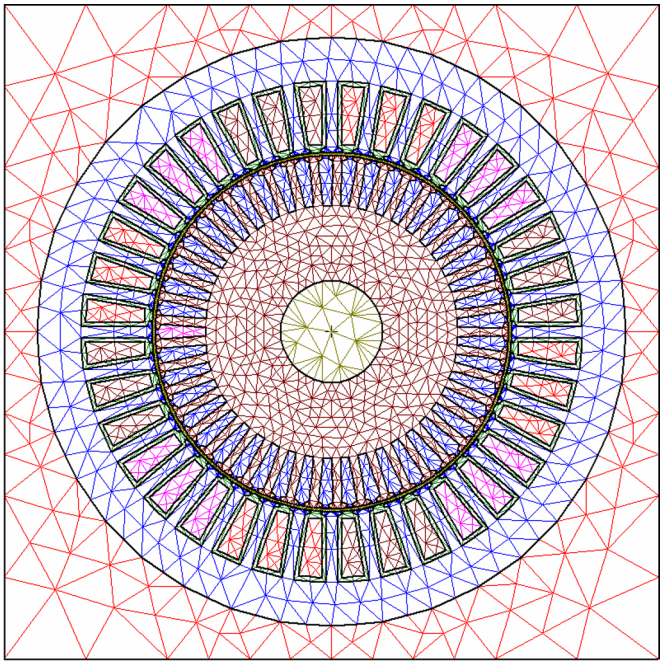

Fig. 6. Mesh of the FEA model.

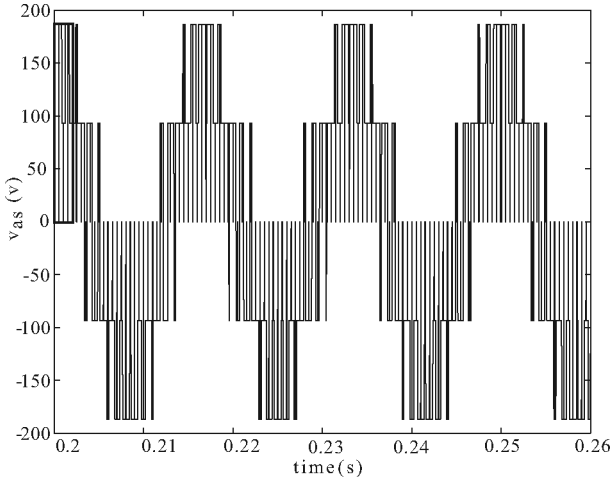

Fig. 7. Phase-a stator voltage that is input to the FEA and MRFCT models.

with third-harmonic injection is used for control of the inverter switching. The dc supply voltage of the inverter is 280 V. The duty cycles for the three phases are of the form

$$d_a = d\cos(\theta_c) - \frac{d\cos(3\theta_c)}{6} \tag{43}$$

$$d_b = d\cos(\theta_c - 2\pi/3) - \frac{d\cos(3\theta_c)}{6} \tag{44}$$

$$d_c = d\cos(\theta_c + 2\pi/3) - \frac{d\cos(3\theta_c)}{6} \tag{45}$$

where $d = 2/\sqrt{3}$ [22]. In this paper, $\theta_c = 120\pi t$. The switching frequency was set to 1 kHz.

For the comparison of performance, a commercial FEA package Ansoft Maxwell 2-D Version 10 was used to implement an FEA model of the induction machine. It was also used to establish the basis functions for the MRFCT model. The mesh of the FEA model is shown in Fig. 6 and contains 11,118 triangles that use linear polynomials as the approximation function. The input to the FEA was the stator winding voltages that are obtained using (35)–(37). Within the FEA, a fixed time-step Newton–Raphson method coupled with the incomplete Cholesky-conjugate gradient algorithm was applied [26]. A backward-Euler method, with a fixed time step of 0.01 ms was used for the numerical integration. The tolerance on the FEA solve was set to be 0.001 for the linear residual and 0.005 for the nonlinear residual. The local virtual work method is used within the FEA algorithm to calculate the electromagnetic torque.

The MRFCT program was implemented within the commercial software MATLAB. A step size of 1 ms was used for the low-frequency FC and 0.01 ms was used for the high-frequency FC. The number of samples used in the convolution evaluation for the high frequency response was $N_f = 100$.

Prior to describing the simulation setup further, it is useful to consider the selection of the respective time steps. First, a 1 ms was selected to capture the low-order dynamics that include the dominant magnetomotive force (MMF) (1st–7th) harmonics and the slower time constants of the rotor circuit. The 1 ms time step corresponds to a sampling rate of 1 kHz for the low-frequency waveforms, and thus, the highest frequency at which the slow system can portray the response of the system is 500 Hz. The 0.01 ms time step for the fast subsystem leads one to believe that the system is oversampled, given the 1 kHz switching frequency. However, it has been found that some degree of oversampling of the fast system provides user flexibility. Specifically, there is often a desire to investigate the performance of the machine/inverter under a range of switching frequencies. If in the high-frequency impulse response, the system is oversampled (within reason), then a single impulse response can be used to evaluate the performance of the machine/inverter under a range of switching frequencies. As an example, for the 1 kHz application, the high frequency response is calculated over a switching-cycle interval using $N_f = 100$ of the high-frequency impulse response. If the performance of the system is desired under a switching frequency of 10 kHz, then the same high-frequency impulse response can be used with $N_f = 10$. If the performance of the system under various switching frequencies is not of interest, there is no need to oversample the high-frequency impulse response. This also highlights an important point of the proposed technique—the computational effort of the MRFCT does not increase with switching frequency.

For both FEA and MRFCT, the stator resistance was set to $r_s = 1.2\ \Omega$ and it was assumed the machine was operated at a fixed speed of 1760 r/min. A 3.19 GHz PC was used to perform both the FEA and MRFCT evaluations. The stator voltage that was applied to both models is shown in Fig. 7. In Figs. 8–11, the induction machine performance predicted by the FEA and MRFCT is compared. The performance results include the time and frequency responses of the phase-a stator current and the electromagnetic torque in the time and frequency domains.

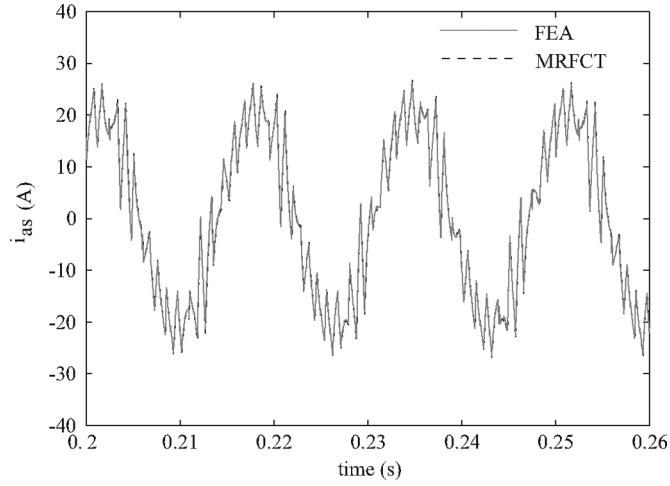

Fig. 8. Phase-a stator current.

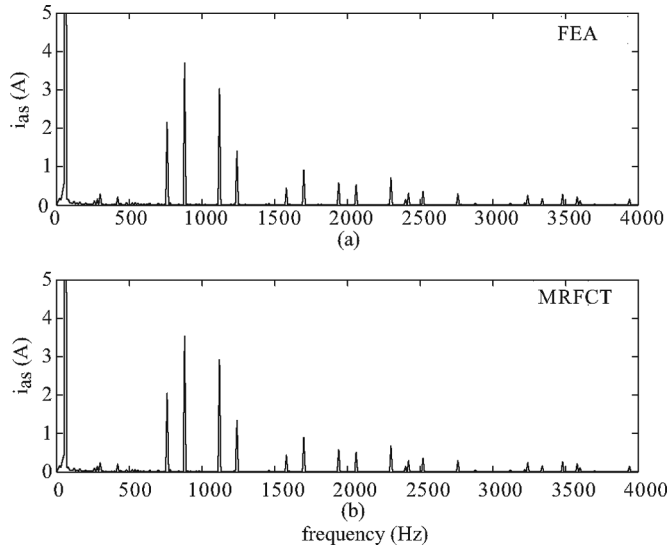

Fig. 9. Phase-a stator current frequency spectrum.

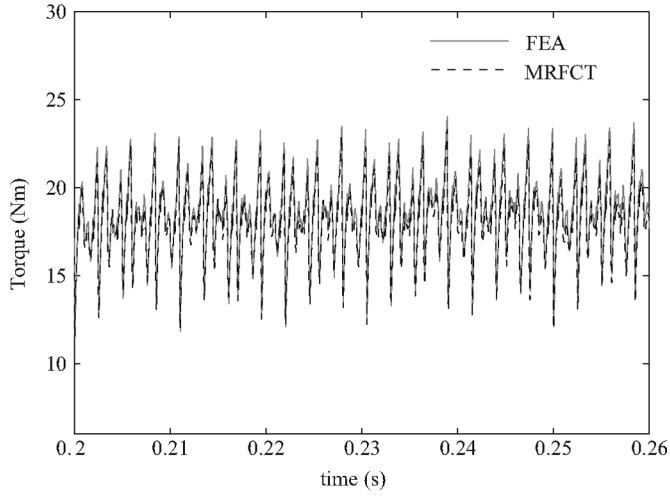

Fig. 10. Electromagnetic torque.

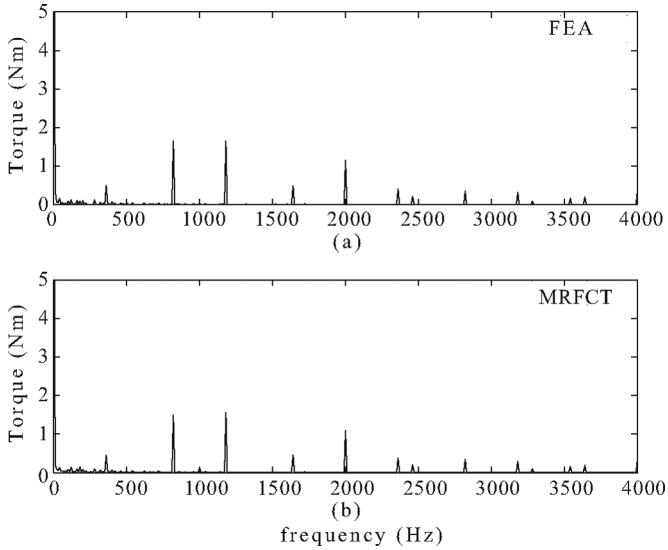

Fig. 11. Electromagnetic torque ripple spectrum. (a) FEA. (b) MRFCT.

The Maxwell stress tensor method was used to calculate torque using (4). As part of the evaluation of torque, the flux densities were calculated at 999 points in the airgap (i.e., $p = 999$). With the time step of 1 ms, the convolution calculations within (14) require $O(999 \times 1000^2)$ *computations per second of simulated response for the slow subsystem* (for the 0.06 s time interval shown, the computations required $O(999 \times 60^2)$). With $N_f = 100$, and $p = 999$, the convolution calculations within (41) are fixed at $O(999 \times 100^2)$ since the convolution is truncated.

To compute the responses, the FEA required roughly 207 h/s *of simulation time* (745,200 times slower than real time). In contrast, the MRFCT model required 40 min/s of simulated response (2400 times slower than real time). A traditional voltage-input-based FCT without partitioning fast and slow components (time step 0.01 ms), with $p = 999$ would require on the order of $O(999 \times 100000^2)$ computations to perform the convolution calculations in (14) *per second of simulated response*. Thus, the traditional voltage-input-based FCT model would be on the order of ten thousand times slower than the MRFCT, and even slower than the FEA model.

Despite the fact that the MRFCT solved at a rate that is orders of magnitude faster, it is observed that the model response is nearly identical to that obtained by the FEA in both the time and frequency domains over a very wide bandwidth. The gain in simulation speed without sacrifice in accuracy greatly enhances the usefulness of field-based modeling as part of the machine design and analysis process.

VI. Brief Discussion

Since there are a number of techniques used to model induction machines, it is helpful to briefly highlight differences between MRFCT and more traditional lumped parameter and magnetic equivalent circuit (MEC) models. Undoubtedly, lumped parameter and MEC models will require less computational effort to perform a time-domain simulation than the

MRFCT. Researchers have shown near real-time simulation of machine/inverters using lumped parameter models [27]. However, a challenge in lumped parameter and MEC models is to capture the distributed nature of the rotor. Researchers have presented a host of techniques to augment traditional q-d models [28]–[35]. However, the effort required to determine model parameters is significant. If one follows the modeling approach proposed in [28] (MMF harmonics are neglected in the model presented therein), a transient FEA simulation at different speeds and load conditions (with rotor rotation) is required to determine the parameters. Determining model parameters becomes more complicated if harmonics due to stator and rotor windings are to be included along with a distributed rotor representation [29]. In addition, if one attempts to generate model parameters from a machine geometry (i.e., using winding functions or flux tubes), determining the impact of slotting and the accurate calculation of stator and rotor leakage inductances always presents a challenge. Both have potentially significant impact on the current harmonics, and thus, the torque harmonics.

Although saturation is not included in the MRFCT, a convenience is that the distributed nature of the rotor system, winding harmonics, stator and rotor slots, and leakage paths are represented. In addition, the characterization procedure is relatively straightforward-–there is no rotation required and a simple input is used. Moreover, the computational effort does not increase with switching frequency. Although not detailed herein, if one characterizes basis functions in the iron, one can extend the MRFCT to include core loss calculation. One can also readily apply the machine to other machine types where analytical calculation of the flux behavior is a challenge, i.e., slotless or air core stators, etc.

Although the MRFCT is derived based upon linearity assumptions, there may be means to account for saturation in this model that is similar to that of other lumped parameter models. Specifically, it may be possible to express the basis function amplitudes as a function of flux density values, which is similar to adjusting magnetizing inductance based upon magnetizing flux linkage in lumped parameter models. This is the topic of ongoing research.

Of final note is that the MRFCT approach does require a separation of time scales. This may not always exist. For example, if a machine has a stator or rotor winding or slot structure that yields appreciable harmonics in flux densities near the switching frequency, the underlying assumptions used to develop MRFCT break down. As switching frequencies tend to increase, the likeliness of this would appear to diminish.

VII. Conclusion

A multirate FCT has been developed to efficiently model the fields and forces within induction machines fed by power electronic inverters. The stator currents are partitioned into low- and high-frequency components. Two FCs are performed (low- and high-frequency) in which different step sizes are used to calculate the respective dynamics. To illustrate the proposed MRFCT, an induction machine driven by sine–triangle PWM with third harmonics is considered. The results are validated using FEA. It is observed that the MRFCT provides satisfactory accuracy with only a small fraction of time compared to FEA.

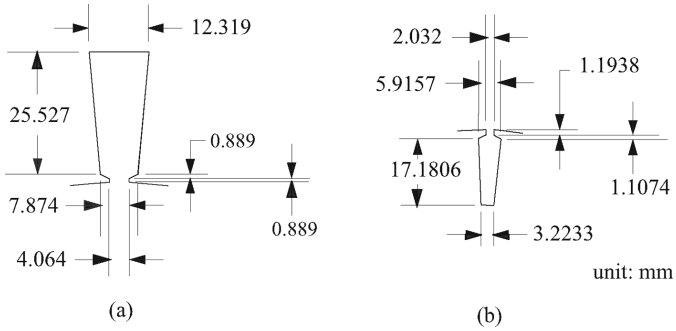

Fig. 12. Dimension of stator and rotor slots. (a) Stator slot. (b) Rotor slot.

Appendix A

The dimensions of stator and rotor slots are shown in Fig. 12. The parameters of the machine studied are listed in Table I.

TABLE I
Induction Machine Parameters

Rated voltage V=208 V rms L-L	Rated speed ω_{rm}=1760 rpm	Rated torque T_e=20.23 Nm
Airgap g = 1.42 mm	Rotor outer diameter d_r=136.92 mm	Stator outer diameter d_s=228.6 mm
Stack length l =88.9 mm	Shaft diameter d_{shaft}=39.4 mm	Lamination material M-19
Stator winding material copper	Rotor bar material Aluminum	Number of coils/phase 6 coils in series connection

Appendix B

In this research, the impulse response is used to characterize the relationship between stator input and the flux densities due to the rotor. Moreover, convolution of the stator current and impulse response is used to establish the flux densities due to arbitrary stator current. Convolution and the impulse response are concepts used frequently in communications and signal processing. In contrast, it has been used sparingly as a basis for machines/drives research. Thus, it is convenient to provide some background on these topics.

The models developed herein are implemented digitally, and thus, it is convenient to consider these topics in discrete time. The output of a discrete-time linear time-invariant (LTI) system can be expressed as

$$y(k) = \sum_{m=0}^{k} a(m)u(k-m) \tag{46}$$

where a is the output of the system obtained due to a unit impulse. The discrete-time unit impulse signal is defined as

$$u(k) = \begin{cases} 1, & k = 0 \\ 0, & k \neq 0. \end{cases} \tag{47}$$

In many texts, the summation of (46) is denoted with $y(k) = a(k) * u(k)$. To explain the practical implementation of (46) and provide some physical meaning, it is convenient to compute

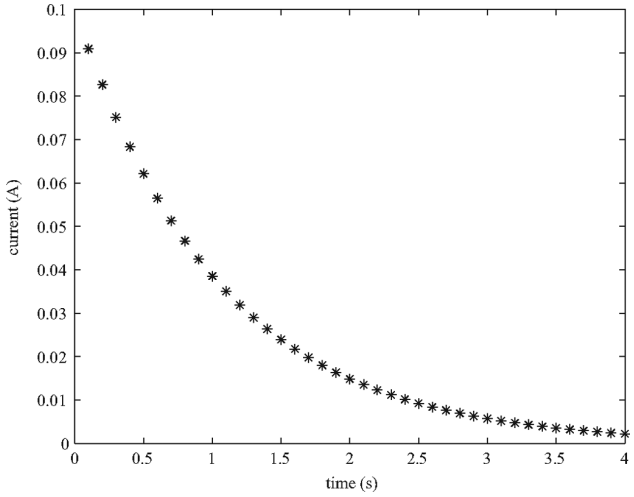

Fig. 13. Impulse response of r–$L(1\ \Omega, 1\ \text{H})$ system $h = 0.1$s.

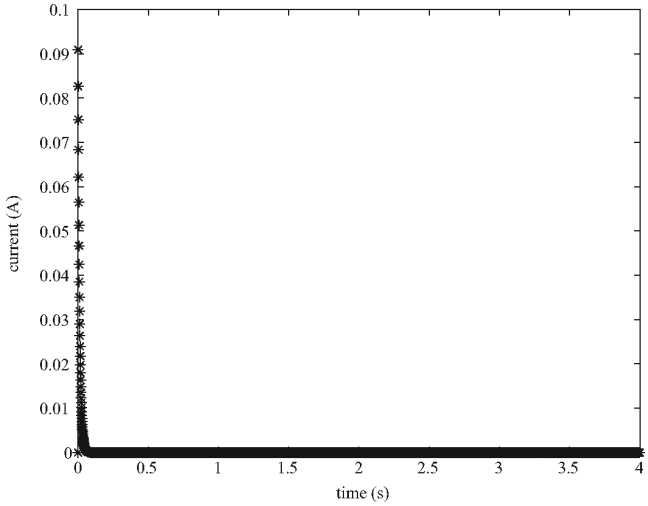

Fig. 14. Impulse response of r–$L(1\ \Omega, 10\ \text{mH})$ system $h = 1$ ms.

the impulse response of a model of an *r–L* circuit. To start, the dynamics of a series *r–L* circuit can be represented in the continuous time as

$$\frac{di}{dt} = \frac{v}{L} - \frac{ri}{L}. \tag{48}$$

Discretization of (48) using an ordinary differential equation (ODE) algorithm results in an LTI discrete-time system. The form of the discrete equation depends on the integration algorithm selected. Using a forward-Euler algorithm results in a model of the form

$$i(k+1) = i(k)(1 - rh/L) + hv(k)/L \tag{49}$$

where h is the time step. The impulse response of (49) is obtained by setting $v(k)$ according to (47) and solving with this input. The initial value of the current $i(0)$is assumed to be zero. It is noted that this is considered an approximate impulse response, since it does not account for the zero time width of a true impulse (i.e., the impulse is technically applied over a time step) [37]. Methods of accounting for a zero-width impulse response exist for a broad class of systems described in [37]. However, these methods are not directly applicable for the MRFCT considered herein, and thus, are not described further.

To illustrate their behavior, impulse responses were obtained for the system of (49), with two sets of parameter values. In the first response, $r = 1\ \Omega$, $L = 1$ H. The time step used to compute the response was 0.1 s. In the second, $r = 1\ \Omega$ and $L = 10$ mH, and the time step was 1 ms. Plots of the responses are shown in Figs. 13 and 14.

In both Figs. 13 and 14, one can see that the impulse response reflects the time constant of the respective system. Specifically, in Fig. 13, the impulse response decays at a rate consistent with an r–L time constant of 1 s. In Fig. 14, the rate of decay is much faster (r–L time constant is 10 ms).

In general, a system with fast dynamics will have an impulse response that decays rapidly with time. Thus, the most important components of the impulse response of a fast dynamic system are over the short time interval following the application of the impulse. The sampling rate must be sufficient to capture these; the values following the initial decay have little impact on the output. In contrast, a slow dynamic system has an impulse response that decays much slower. To compute the output, the convolution must be taken over a longer interval of time. In contrast to the fast system, a high sampling rate is not needed since the system decays relatively slowly. Further information on the impulse response is provided in [38].

In the application of the induction machine considered herein, a complication is that the system contains both high- and low-frequency dynamics (and inputs). The partitioning described in Section IV is used to overcome this hurdle.

A further question is whether LTI theories can be applied since the machine is time-varying. Herein, LTI theories are applied to compute the impulse response of the machine at standstill. Neglecting saturation, the system at standstill is indeed LTI. Reference frame theory is then used to create a model in which the LTI-based model parameters are used to model the machine that includes rotor motion in a manner that is analogous to the way it is used in the development of *q–d* models that are position-independent.

REFERENCES

[1] S. Williamson and M. C. Begg, "Analysis of cage induction motors—A combined fields and circuits approach," *IEEE Trans. Magn.*, vol. MAG-21, no. 6, pp. 2396–2399, Nov. 1985.

[2] A. Smith, S. Williamson, and J. Smith, "Transient currents and torques in wound-rotor induction motors using the finite element method," *Proc. Inst. Electr. Eng.*, vol. 137, no. 3, pp. 160–173, May 1990.

[3] N. A. Demerdash, J. F. Bangura, and A. A. Arkadan, "A time-stepping coupled finite-element state-space modeling environment for induction motor drives—part I: Model formulation and machine parameter computation," *IEEE Trans. Energy Convers.*, vol. 14, no. 4, pp. 1465–1471, Dec. 1999.

[4] J. F. Bangura, F. N. Isaac, N. A. Demerdash, and A. A. Arkadan, "A time-stepping coupled finite-element state-space modeling environment for induction motor drives—part II: Machine performance computation and verification," *IEEE Trans. Energy Convers.*, vol. 14, no. 4, pp. 1472–1478, Dec. 1999.

[5] E. Strangas, "Coupling the circuit equations to the non-linear time dependent field solution in inverter-driven induction motors," *IEEE Trans. Magn.*, vol. MAG-21, no. 6, pp. 2408–2411, Nov. 1985.

[6] A. Arkkio, "Finite element analysis of cage induction motors fed by static frequency converters," *IEEE Trans. Magn.*, vol. 26, no. 2, pp. 964–969, Mar. 1990.

[7] T. W. Preston, A. B. J. Reece, and P. S. Sangha, "Induction motor analysis by time-stepping techniques," *IEEE Trans. Magn.*, vol. 24, no. 1, pp. 471–474, Jan. 1988.
[8] S. Williamson, L. H. Lim, and M. J. Robinson, "Finite-element models for cage induction motor analysis," *IEEE Trans. Ind. Appl.*, vol. 26, no. 6, pp. 1007–1017, Nov./Dec. 1990.
[9] N. A. Demerdash and P. Baldassari, "A combined finite-element state-space modeling environment for induction motors in the ABC frame of reference-part I: The no load condition," *IEEE Trans. Energy Convers.*, vol. 7, no. 4, pp. 698–709, Dec. 1992.
[10] N. A. Demerdash and P. Baldassari, "A combined finite-element state-space modeling environment for induction motors in the ABC frame of reference—part II: The blocked rotor and sinusoidally energized load conditions," *IEEE Trans. Energy Convers.*, vol. 7, no. 4, pp. 710–720, Dec. 1992.
[11] S. L. Ho and W. N. Fu, "A comprehensive approach to the solution of direct-coupled multislice model of skewed rotor induction motors using time-stepping eddy current finite element method," *IEEE Trans. Magn.*, vol. 33, no. 3, pp. 2265–2273, May 1997.
[12] L. Xu and E. Ruckstadter, "Direct modeling of switched reluctance machine by coupled field-circuit method," *IEEE Trans. Energy Convers.*, vol. 10, no. 3, pp. 446–454, Sep. 1995.
[13] M. J. Kamper, S. W. Rasmeni, and R. J. Wang, "Finite-element time-step simulation of the switched reluctance machine drive using single pulse mode operation," *IEEE Trans. Magn.*, vol. 43, no. 7, pp. 3202–3208, Jul. 2007.
[14] S. Williamson and A. F. Volschenck, "Time-stepping finite element analysis for a synchronous generator feeding a rectifier load," *Proc. Inst. Electr. Eng. Electr. Power Appl.*, vol. 142, no. 1, pp. 50–56, Jan. 1995.
[15] P. Eustache, G. Meunier, and J. L. Coulumb, "Finite element toolbox for generic coupling," *IEEE Trans. Magn.*, vol. 32, no. 3, pp. 1461–1464, May 1996.
[16] P. Kuo-Peng, N. Sadowski, J. P. A. Bastos, R. Carlson, and N. J. Batistela, "A general method for coupling static converters with electromagnetic structures," *IEEE Trans. Magn.*, vol. 33, no. 2, pp. 2004–2009, Mar. 1997.
[17] P. Zhou, D. Lin, W. N. Fu, B. Ionescu, and Z. J. Cendes, "A general cosimulation approach for coupled field-circuit problems," *IEEE Trans. Magn.*, vol. 42, no. 4, pp. 1051–1054, Apr. 2006.
[18] I. A. Tsukerman, A. Konrad, G. Meunier, and J. C. Sabonnadière, "Coupled field-circuit problems: Trends and accomplishements," *IEEE Trans. Magn.*, vol. 29, no. 2, pp. 1701–1704, Mar. 1993.
[19] D. Wu, S. D. Pekarek, and B. Fahimi, "A field reconstruction technique for efficient modeling of the fields and forces within induction machines," *IEEE Trans. Energy Convers.*, vol. 24, no. 2, pp. 366–374, Jun. 2009.
[20] D. Wu, "A field construction technique to efficiently model the dynamic vector forces within induction machines," Ph.D. dissertation, School Electr. Comput. Eng., Purdue Univ., West Lafayette, IN, 2008.
[21] D. Wu, S. D. Pekarek, and B. Fahimi, "A voltage-input-based field reconstruction technique for efficient modeling of the fields and forces within induction machines," *IEEE Trans. Ind. Electron.*, to be published.
[22] P. C. Krause, O. Wasynczuk, and S. D. Sudhoff, *Analysis of Electric Machinery and Drive Systems*. Piscataway, NJ: IEEE Press, 2002, ch. 13, pp. 483–487.
[23] S. J. Salon, *Finite Element Analysis of Electrical Machines*. Norwell, MA: Kluwer, 1995.
[24] A. Koski, K. Forsman, T. Tarhasaari, J. Kangas, and L. Kettunen, "Force and torque computations with hybrid methods," *IEEE Trans. Magn.*, vol. 35, no. 3, pp. 1387–1390, May 1999.
[25] A. V. Oppenheim, A. S. Willsky, and S. H. Nawab, *Signals and Systems*, 2nd ed. ed. Upper Saddle River, NJ: Prentice-Hall, 1997.
[26] *Maxwell 2D Field Simulator Manuals*. Pittsburgh, PA: Ansoft Corporation, 2002.
[27] C. Dufour and J. Belanger, "A real-time simulator for doubly fed induction generator based wind turbine applications," *Proc. Power Electron. Spec. Conf.*, vol. 5, no. 3, pp. 3597–3603, Jun. 2004.
[28] S. D. Sudhoff, D. C. Aliprantis, B. T. Kuhn, and P. L. Chapman, "An induction machine model for predicting inverter–machine interaction," *IEEE Trans. Energy Convers.*, vol. 17, no. 2, pp. 203–210, Jun. 2002.
[29] H. R. Fudeh and C. M. Ong, "Modeling and analysis of induction machines containing space harmonics. Part I: Modeling and transformation," *IEEE Trans. Power App. Syst.*, vol. PAS-102, no. 8, pp. 2608–2615, Aug. 1983.
[30] W. Levy, C. F. Landy, and M. D. McCulloch, "Improved models for the simulation of deep bar induction motors," *IEEE Trans. Energy Convers.*, vol. 5, no. 2, pp. 393–400, Jun. 1990.
[31] E. Levi, "Main flux saturation modeling in double-cage and deep-bar induction machines," *IEEE Trans. Energy Convers.*, vol. 11, no. 2, pp. 305–311, Jun. 1996.
[32] A. C. Smith, R. C. Healey, and S. Williamson, "A transient induction motor model including saturation and deep bar effect," *IEEE Trans. Energy Convers.*, vol. 11, no. 1, pp. 8–15, Mar. 1996.
[33] J. Langheim, "Modeling of rotor bars with skin effect for dynamic simulation of induction machines," in *Proc. IEEE Ind. Appl. Soc. Annu. Meeting*, 1989, pp. 38–44.
[34] I. Boldea and S. A. Nasar, "A general equivalent circuit (GEC) of electric machines including cross coupling saturation and frequency effects," *IEEE Trans. Energy Convers.*, vol. 3, no. 3, pp. 689–695, Sep. 1988.
[35] X. Luo, H. A. Toliyat, A. El-Antably, and T. A. Lipo, "Multiple coupled circuit modeling of induction machines," *IEEE Trans. Ind. Appl.*, vol. 31, no. 6, pp. 311–318, Mar./Apr. 1995.
[36] A. R. Muñoz and T. A. Lipo, "Complex vector model of the squirrel-cage induction machine including instantaneous rotor bar currents," *IEEE Trans. Ind. Appl.*, vol. 35, no. 3, pp. 1332–1340, Nov./Dec. 1999.
[37] MATLAB Technical Notes on Convolution. [Online]. Available: http://www.mathworks.com/support/tech-notes/1900/1901.html
[38] R. Gabel and R. Roberts, *Signals and Linear Systems*, 3rd ed. New York: Wiley, 1986.

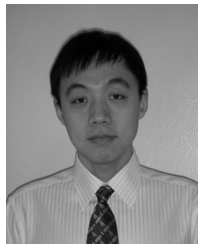

Dezheng Wu received the B.Eng. degree in electrical engineering from Shanghai Jiao Tong University, Shanghai, China, in 2000, the M.Eng. degree from the National University of Singapore, Singapore, in 2005, and the Ph.D. degree in electrical engineering from Purdue University, West Lafayette, IN, in 2008.

He is currently a Power Electronics R&D Engineer at the ABB US Corporate Research Center, Raleigh, NC. His current research interests include design, analysis, and control of electric machines.

Steven D. Pekarek (S'89–M'96) received the Ph.D. degree in electrical engineering from Purdue University, West Lafayette, IN, in 1996.

From 1997 to 2004, he was an Assistant (Associate) Professor of electrical and computer engineering at the University of Missouri Rolla (UMR), Rolla. He is currently a Professor of electrical and computer engineering at Purdue University and is the Chair of the energy sources and systems area. As a faculty member, he has been the Principal Investigator on a number of successful research programs including projects for the Navy, Air Force, Ford Motor Company, Motorola, and Delphi Automotive Systems. The primary focus of these investigations has been the analysis and design of power-electronic-based architectures for finite inertia power and propulsion systems.

Prof. Pekarek is an active member of the IEEE Power Engineering Society, the Society of Automotive Engineers, the IEEE Power Electronics Society, and Chair of the 2008 IEEE Applied Power Electronics Conference. At UMR, he was the recipient of six Outstanding Teaching Commendations and four Faculty Excellence Awards.